

# A Machine Learning Approach for Multiscale Modeling of Biological Tissues

**Nishan Parvez**

Department of Mechanical Aerospace and  
Nuclear Engineering,  
Rensselaer Polytechnic Institute,  
110 8th Street,  
Troy, NY, USA

**Jacob S. Merson<sup>1</sup>**

Department of Mechanical Aerospace and  
Nuclear Engineering,  
Rensselaer Polytechnic Institute,  
110 8th Street,  
Troy, NY, USA  
email: merso2@rpi.edu

*We develop a new neural network architecture that strictly enforces constitutive constraints such as polyconvexity, frame-indifference, and the symmetry of the stress and material stiffness. Additionally, we show that the accuracy of the stress and material stiffness predictions is significantly improved for this neural network by using a Sobolev minimization strategy that includes derivative terms. Using our neural network, we model the constitutive behavior of fibrous-type discrete network material. With Sobolev minimization, we obtain a normalized mean square error of 0.15% for the strain energy density, 0.815% averaged across the components of the stress, and 5.4% averaged across the components of the stiffness tensor. This machine-learned constitutive model was deployed in a finite element simulation of a facet capsular ligament. The displacement fields and stress-strain curves were compared to a multiscale simulation that required running on a GPU-based supercomputer. The new approach maintained upward of 85% accuracy in stress up to 70% strain while reducing the computation cost by orders of magnitude.*

*Keywords: multiscale analysis, facet capsular ligament, machine learning, constitutive relation, surrogate model*

## 1 Introduction

Biological systems are among the most complicated to model, with the relevant lengths and timescales spanning more than nine orders of magnitude. This complexity has led to the emergence of various multiscale methodologies that enable a greater understanding of the interplay between scales. They are gaining particular traction in modeling biological tissues that are often made of collagen fibers [1–3].

An upscaling multiscale approach is typical for modeling biological tissues because there is a strong scale separation between the macroscale and microscale length scales. In these methods, the microscale material behavior is homogenized to provide the constitutive properties for the macroscale analysis. This homogenization can either be done concurrently with the macroscale solution, or a priori.

In a priori homogenization, simulations are typically used to perform a standard set of computational experiments (e.g., uniaxial displacement, biaxial displacement, pure shear, etc.) to calibrate a constitutive model such as the HGO, or Fung model [4]. This is computationally inexpensive because the set of numerical experiments needed is kept to a minimum. However, traditional analytical constitutive response functions often do not contain enough degrees of freedom to capture behaviors that stem from micromechanical fields that contain non-affinity, and non-locality. One such observed emergent behavior is that networks exhibit Poisson's ratios over the thermodynamic limit for homogeneous elastic materials [5].

Another option is to use an upscaling multiscale method where the microstructure is homogenized concurrently with the solution of the macroscale. One example of this homogenization scheme is the FE<sup>2</sup> method developed by [6] and others. This mitigates the need for an analytical constitutive response function and can handle a broader range of emergent behaviors. However, this method is computationally expensive, and realistic problem sizes require the use of supercomputers and specialized solution procedures [7].

In both cases, these hierarchical methods require strong scale

separation and homogenization over a domain that is large enough to have representative material properties. In the homogenization literature, this is typically described as the size where the constitutive response remains unchanged under equivalent loading conditions (e.g., the Voigt and Reuss bounds converge).

In 3D Voronoi networks, a common proxy for collagen networks, the RVE size is  $\gg 40$  times the mean fiber length ( $l_c$ ) [8]. In this work, we take the standard definition of the RVE. However, simulations of this size are not tractable in the context of upscaling multiscale analysis without the use of specialized numerical algorithms and supercomputers. The problem is exacerbated by the incorporation of inclusions (such as cells) or the interaction of multiple fiber types, which increases the length scale of heterogeneity. Unfortunately, these situations are ubiquitous in tissue modeling [2].

Due to this cost, the most common approach is to use a priori homogenization methods. The analytical material models for fibrous structures are based on the affine assumption that the end-to-end vector of the fiber will deform according to a global deformation gradient. Many authors have shown that the nonaffine behavior of stochastic networks is critical to the overall response [9–13]. In this paper, we show that machine learning models are able to accurately capture the material response and better account for the nonaffine behavior of network materials.

Over the past ten years, machine learning models have become an increasingly important part of the engineering design process. Showing promise in predicting complex deformation fields and in constitutive modeling of nonlinear materials [14–17]. When used naively, machine learning models do not obey important constitutive axioms such as material frame indifference and polyconvexity.

In this paper, we develop a novel neural network architecture based on the fully connected Input Convex Neural Network [18]. Additionally, we show that when learning the response of hyperelastic materials, it is not sufficient to train with the energy functional alone, but must use a Sobolev type minimization scheme that accounts for the stress and derivative quantities. Finally, we provide direct examples where these surrogate constitutive models can be used to replace expensive multiscale computations of the facet capsular ligament which are performed on large heterogeneous su-

<sup>1</sup>Corresponding Author.

Version 1.18, May 20, 2024

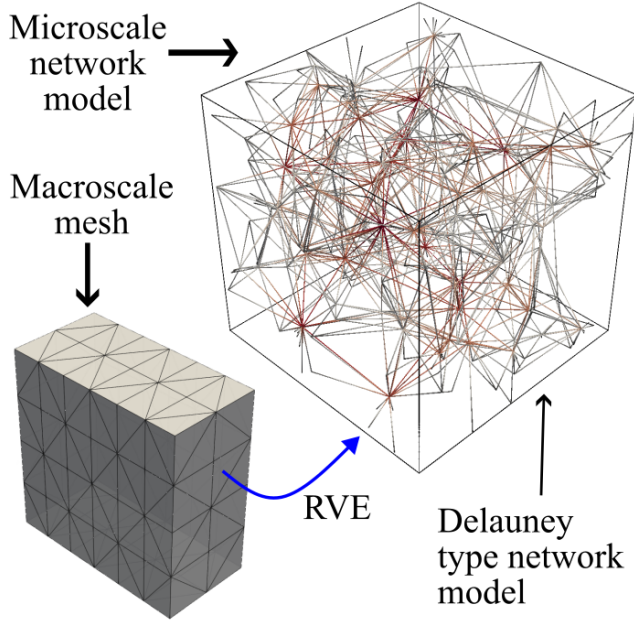


**Fig. 1 Schematic of a single Delaunay network (RVE) realization. In the upscaling FEM method, an RVE is solved at every integration point to compute the stress and material stiffness given an increment in macroscale strain.**

percomputers.

## 2 Methods

### 2.1 Multiscale Finite Element Method.

**2.1.1 Macroscale Problem.** On the macroscale, we use an updated-Lagrangian displacement based finite element formulation where we solve the balance of virtual power.

$$\delta P = \delta P^{\text{int}} - \delta P^{\text{ext}} = 0 \quad \forall \delta \mathbf{v} \in \mathcal{v} \quad (1)$$

where

$$\delta P^{\text{int}} = \int_V \sigma_{ij} \delta D_{ij} dV, \quad (2)$$

$$\delta P^{\text{ext}} = \int_{\partial V} \mathbf{t}_i \delta v_i d\Gamma. \quad (3)$$

Here,  $\mathcal{v}$  is the set of kinematically admissible velocity fields,  $\sigma$  is the Cauchy stress,  $\mathbf{D}$  is the symmetric rate of deformation tensor,  $\mathbf{t}$  is the surface traction,  $V$  is the total volume of the body, and  $\partial V$  is the surface of the domain.

By pulling out the virtual velocities from the integrals and noting the arbitrariness of the virtual velocities, we obtain the typical nonlinear discretized equations for the residual

$$\mathcal{R}_{kI} = \int_V B_{ijkl} \sigma_{ij} dV - \int_{\partial V_j} N_I t_k d\Gamma_j = 0, \quad (4)$$

and the tangent stiffness

$$K_{kI r J} = \int_V B_{ijkl} \mathbb{D}_{ijpq} B_{pqr J} dV + \delta_{ij} \int_V B_{ijkl} \sigma_{pq} B_{pqr J} dV, \quad (5)$$

where majuscule indices correspond to nodal degrees of freedom, and minuscule indices correspond to spatial dimensions,  $\mathbf{B}_J$  is the shape function derivatives at node  $I$ ,  $N_I$  is the shape functions at node  $I$ ,  $\mathbb{D}$  is the tangent material stiffness. For the updated-Lagrangian finite element procedure, the material stiffness is given as the push forward of the derivative of the second Piola-Kirchhoff with respect to the Green-Lagrange strain. That is,

$$\mathbb{D}_{mnpq} = \frac{1}{J} F_{mi} F_{nj} \frac{\partial \Pi_{ij}}{\partial E_{rs}} F_{pr} F_{qs}. \quad (6)$$

**2.1.2 Multiscale.** In the multiscale problem, the Cauchy stress,  $\sigma$  and tangent material stiffness  $\mathbb{C}$  are computed from a subscale, problem rather than an analytical expression such as the Holzapfel-Gasser-Ogden Model. The inclusion of this subscale problem is what distinguishes the computational method used here from a run-of-the-mill nonlinear finite element method. This methodology is known as a hierarchical or upscaling multiscale method, where we emphasize that the scheme employed here computes subscale problems concurrently with the macroscale solution procedure.

Although we seek a static solution macroscopic solution, an implicit solver does not converge well for RVEs constructed from fiber network materials due to large material nonlinearities. In the fibrous material literature, large strains are typically achieved using dynamic explicit simulations and maintaining the proportion of kinetic energy to strain energy to below five percent. However, multiscale simulations must abide by the Hill-Mandel Criterion, which states that the increment in virtual work held in the subscale problem must match that in the macroscale problem. This means that the microscale problem must be converged such that there is no remaining kinetic energy. To accomplish this, we use the dynamic relaxation procedure that was developed in [1]. Mathematically, this case be stated as:

$$\langle s_{ij} d_{ij} \rangle = \langle s_{ij} \rangle \langle d_{ij} \rangle = \sigma_{ij} D_{ij}, \quad (7)$$

where  $s$  and  $d$  are the stress and rate of deformation tensor computed from the subscale problem, and  $\langle \cdot \rangle = \int_{V^m} \cdot dV^m$  is the volume average.

The Hill-Mandel Criterion can also conveniently be stated as

$$\int_{\partial V^m} \mathbf{t}_i \cdot \delta \dot{h}_i d\Gamma = 0, \quad (8)$$

where  $h_i$  is the microscale fluctuations. In other words, the increment in the virtual work from the boundary fluctuations must go to zero. This second form provides a convenient way to prove if a given boundary condition is valid for use on the microscale.

Three types of boundary conditions are common and abide by the Hill Mandel Criterion: homogeneous displacement, homogeneous traction, and periodic. Many authors argue for the use of periodic boundary conditions because it reduces the size of the RVE that is needed. However, fibrous materials are not periodic, so this choice is not appropriate. Instead, one may use the so called ‘‘Generalized Boundary Condition’’ of [19] which has been extended to fibrous materials [8]. This boundary condition can be used to help mitigate the significant size effect that is present in these materials [8]. In this work, homogeneous displacement boundary conditions are used on the RVE boundaries.

Two key assumptions in the upscaling multiscale formulation are that the subscale problems have behavior that is representative of a macroscale continuum and that the volume of the subscale problem is of a differential size compared with the macroscale finite element within which it resides. These requirements place strict bounds on the size of the RVE.

### 2.1.3 Microscale.

**2.2 Network Generation.** In this work, we use Delaunay fiber networks. The network construction procedure proceeds as follows: First, a generation box is seeded with points using a uniform random distribution. A Delaunay triangularization is constructed from the initial seed points. To avoid boundary effects, the generation box is trimmed so that the new edge length is half of the one used for the generation box. New nodes are inserted at the intersection of the trimming box, and any crossing fibers and any fiber segments that remain outside the trimming box are deleted. This process will yield fiber networks with an average connectivity of  $z = 14$ . This is well above the isostaticity limit for 3D truss networks.

**2.3 Sampling.** One of the major challenges with developing machine learning models is that it is difficult to know if a given input was reasonably covered by the training dataset. We have developed a novel sampling methodology that allows for explicit control over the range of principle stretch values that we may be interested in. This explicit control provides a mechanism to verify if a given deformation state is likely to be covered by the training data.

Since our constitutive response must be frame-indifferent, we can sample the set of positive definite right stretch tensors. The standard relations can be used to map the resulting stress and stiffness back to a rotated frame as needed for the analysis procedures.

We employ the following algorithm to construct our set of positive definite right stretch tensors.

- (1) Sample principle stretches  $\lambda_1, \lambda_2, \lambda_3 \in [\lambda_{\min}, \lambda_{\max}]$ ,  $\lambda_3$  using latin hypercube sampling
- (2) Construct base right stretch tensor

$$\mathbf{U}_i^* = \begin{pmatrix} \lambda_1 & 0 & 0 \\ 0 & \lambda_2 & 0 \\ 0 & 0 & \lambda_3 \end{pmatrix} \quad (9)$$

- (3) Sample a random rotation matrix  $\mathbf{R}_j$
- (4) Construct a realization of the stretch tensor using the polar decomposition formula:

$$\mathbf{U}_j = \mathbf{R}_i \mathbf{U}_i^* \mathbf{R}_j^T \quad (10)$$

- (5) Repeat steps (3)–(4) until sufficient samples are collected for this set of stretches
- (6) Repeat steps (1)–(5) until a sufficient number of base stretches are sampled

If a constant number of samples is used within each ellipsoidal shell that is represented by a given base stretch  $\mathbf{U}_i^*$ , then each data point will cover a varying volume in phase space. To avoid this problem, the number of rotation samples constructed for each set of base stretches is scaled by the surface area of the ellipsoid with  $\lambda_1, \lambda_2, \lambda_3$  forming the ellipsoid axes. This will ensure that, in a statistical sense, each sampled point will cover a constant volume in phase space, which is critical to avoid oversampling and associated overfitting.

**2.4 Tangent Stiffness.** In this work, we compute the tangent stiffness using a finite difference approach. We have found this to be the most robust approach that works well with our gradient free dynamic relaxation solution procedure [1]. With careful consideration for symmetries, the material stiffness can be computed with only six additional nonlinear solutions to the forward problem. These additional nonlinear solutions are typically inexpensive to obtain because they represent only a small perturbation from the current state.

If Jacobians are available, one can use the reduced stiffness method described in [20], or the Non-affine approach described in [2]. However, typically fiber simulations have significant parts of

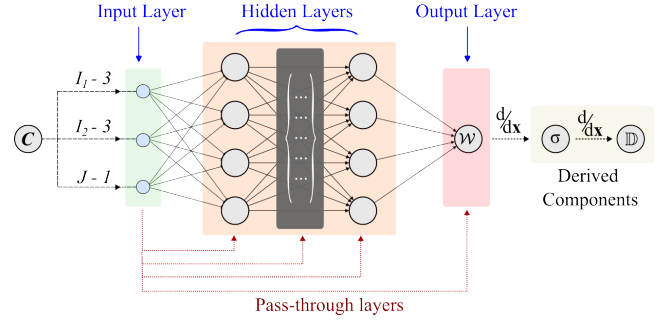


**Fig. 2 Schematic of input convex neural network.** The input vector consists of invariants of the right Cauchy-Green deformation tensor,  $\mathbf{C}$ , and the output is the predicted strain energy density,  $\mathcal{W}$ . The components of true stress,  $\boldsymbol{\sigma}$ , and stiffness tensor,  $\mathbb{D}$ , are computed using automatic differentiation of the trained model.

the load path that have singular Jacobians due to nonlinearities so these methods are not feasible, despite the potential performance improvement.

**2.5 Machine Learning Model.** The majority of the computational cost in the multiscale method is incurred in the distributed parallel analysis of RVEs owing to the lack of an analytical constitutive model [1]. The primary contribution of this work is toward providing a neural network-based framework that will approximately model the fibrous network material. Therefore, the trained model can act as a drop-in replacement of microscale simulations, which reduces the FE<sup>2</sup> method to the traditional FE algorithm that executes at a fraction of the computational cost of the MuMFiM[1]. To this end, we assume the material behavior is hyperelastic up to the point of failure, which is supported by numerical and experimental results [4,21,22].

The hyperelastic formulation entails finding a non-negative, non-decreasing, and convex scalar energy density function,  $\mathcal{W}$ , in terms of deformation-related quantities [23,24]. The stress and stiffness tensor components are then found through appropriate first and second-directional derivatives of  $\mathcal{W}$ . The convexity condition implies the machine learning algorithm must be chosen or designed appropriately [18,25]. Here, we employ the Input Convex Neural Network (ICNN) model, which guarantees that the overall mathematical form of the neural network will be convex for the proper choice of input and output quantities. The ICNN network was originally pioneered in [18]. Various authors have used the ICNN as a basis for hyperelastic material modeling [14,24–27]. A schematic of the neural network model we implemented is shown in Figure 2.

ICNN is a particular form of fully connected neural network with restrictions on activation functions and weights. The convexity of the model is ensured by strictly adhering to (i) convex activation functions and (ii) non-negative weights. While the first requirement is trivial, non-negative weights limit the scope of the neural network when modeling complex phenomena [18]. To counter, a number of pass-through layers without restrictions on weights or biases are introduced that connect the input to the hidden layer neurons. These pass-through layers amount to affine mapping of input to hidden layer neurons. Therefore, if the ICNN output is a convex function of the input, the convexity condition on the strain energy density function is satisfied by construction.

Here, we aim to map the principal invariants of the Right Cauchy-Green deformation tensor to the deformed material's strain energy density through ICNN. Following [27], the input layer of ICNN consists of modified invariants of the right Cauchy-Green deformation tensor— $I_1 - 3$ ,  $I_2 - 3$ , and  $I_3 - 1$ —this choice helps to normalize the input values. We employ the *Soft Plus* activation function defined as  $g(x) = 1/\beta \log(1 + \beta \exp(x))$  with  $\beta = 1$ ,

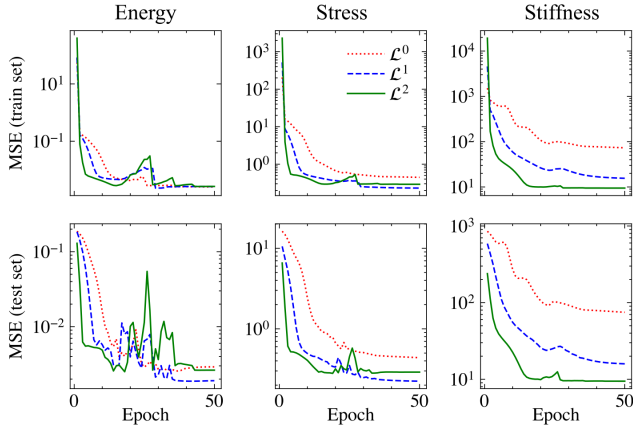


**Fig. 3** Mean squared error (loss) of ICNN during training. The average errors associated with strain energy density, stress, and stiffness tensors are shown in the first, second, and third column, respectively. The top row shows the loss for the training dataset, and the bottom row represents the corresponding results for the test dataset. The legend  $\mathcal{L}^k := \sum_{i=0}^k H_i$  indicates the variant of the loss function used to train ICNN, with  $k$  being the highest order of derivative included in the composite loss function.

a choice inspired by [14,25]. The function is non-negative, non-decreasing, and convex in  $x$ . A second function,  $f$ , of similar characteristics, is applied over the weights to fulfill the requirements for positive weights. Here, we choose  $f = g$  without loss of generality. Therefore, the resulting general form of the strain energy density function is non-negative, non-decreasing, and convex by construction.

This model, however, does not guarantee vanishing strain energy at zero strain, i.e.,  $\mathcal{W}(\mathbf{F} = \mathbf{I}) = 0$  due to the nature of activation functions. This shortcoming, however, can be overcome by the optimization algorithm by adjusting the biases in the pass-through layers. Figure 4 indicates that the requirement is approximately satisfied. An alternative approach can be introducing standalone bias terms to act as correction factors, for example, in [14].

The ICNN we train contains five hidden layers, each having 4 neurons in a fully connected fashion in the primary branch. The pass-through layers connect the input vector to these hidden layer neurons, giving a total of 164 trainable parameters. Mathematically, the output of the neurons in  $i$ -th hidden layer is  $\mathbf{z}^{(i)} = g(f(\mathbf{A}^{(i)}\mathbf{z}^{(i-1)} + \mathbf{A}_p^{(i)}\mathbf{x} + \mathbf{b}_p^{(i)}))$ . Here,  $\mathbf{x}$  is the input vector to the model,  $\mathbf{A}^{(i)}$  is the weight matrix for the  $i$ -th layer of the primary branch. The final two terms,  $\mathbf{A}_p^{(i)}$  and  $\mathbf{b}_p^{(i)}$ , represent the weight matrix and bias vector due to the pass-through connection to  $i$ -th layer, respectively. The model is trained on 91,590 samples with an 80/20 split for the train/test dataset. We use Adams solver for hyperparameter optimization without any weight decay [28]. The model parameters are initialized using Kaiming uniform distribution [29]. We use the mean squared error,  $\text{MSE}(y) = (y_{\text{pred}} - y_{\text{true}})^2$  as the template for the loss function.

In the original and most subsequent implementations of ICNN, the loss function is based on the output variable only. For our purpose, this translates to hyperparameter optimization based on strain energy density. However, due to the large number of trainable parameters, the prediction accuracy for energy does not generally translate to its derivative quantities, such as stress and stiffness, which are necessary for FE simulations. To increase the prediction accuracy of the derivatives, we implement the so-called Sobolev training protocol such that the model is trained on the target output and its derivatives concurrently [30]. Here, we include both the first and second derivatives in the ICNN training procedure as follows.

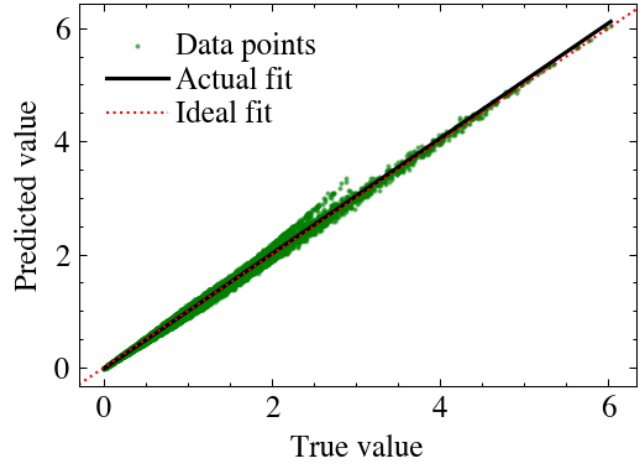


**Fig. 4** True vs predicted strain energy density for the RVEs (test set) based on ICNN trained with  $\mathcal{L}^2$  loss function. The dashed red line indicates the ideal fit, and the solid black line shows the average trend of the predictions. The value of normalized mean squared error is 0.15% for this dataset.

For  $i$ -th batch iteration within an epoch, in addition to the loss in energy,  $H_0 = \text{MSE}(\mathcal{W})$ , we compute the component-average loss in stress,  $H_1 = \langle \text{MSE}(\sigma) \rangle$  and stiffness,  $H_2 = \langle \text{MSE}(\mathbb{D}) \rangle$  through automatic differentiation of the ICNN (updated in  $i-1$ -th iteration). The total loss per batch is computed as  $\mathcal{L}^k = \sum_{j=0}^k H_j$ , with  $k = 2$  being the highest order of derivative considered. The model parameters are then updated based on the computed loss, and the cycle is repeated. The learning rate is adjusted automatically at the end of an epoch based on the mean loss such that the learning rate decreases by a factor of 10 if the loss exhibits a plateau for five consecutive epochs. We use a moderately large batch size so that the loss (especially in the gradients) approximated from a batch is more representative of the population. Finally, we note that the convexity and smoothness of the model are determined by the construction; Sobolev training is an add-on intended for accurate prediction of higher order quantities only.

The neural network model was implemented using the PyTorch [31] framework and is available for public use along with the dataset that the network was trained on<sup>2</sup>. The detailed numerical values of model parameters omitted here for brevity are available in the code repository.

### 3 Results and Discussions

In this section, we first present the model's predictive capability and the improvements brought forth by the Sobolev training protocol. We then present a case study involving mechanical deformation of the Facet Capsule Ligament simulated using the trained model. Finally, we compare the output to the results of MuMFiM based large-scale numerical simulation to comment on the efficacy of the current approach.

**3.1 Sobolev Training of ICNN.** We first discuss the overall predictive accuracy of the input convex neural network, ICNN, in terms of the average loss of desired quantities. This result for energy, stress, and stiffness are shown in the first, second, and third columns of Figure 3. We compare three variants of the model emanating from the choice of the composite loss function, i.e.,  $k = 0, 1, 2$  in  $\mathcal{L}^k = \sum_{j=0}^k H_j$  indicating the highest derivatives

<sup>2</sup>The PyTorch Model, and dataset are available at <https://zenodo.org/doi/10.5281/zenodo.11205879>



included in the loss function. The results are shown in Figure 3 for various quantities of interest.

The first column of Figure 3 shows the loss in strain energy density for different choices of the overall loss function. Expectedly, the choice of loss function has a negligible effect on the predictive accuracy of strain energy density. The derivative quantities, such as stress, however, benefit from including  $H_1$  in the loss function (curves corresponding to  $\mathcal{L}^1$ ). This result is shown in the second panel of Figure 3. This additional information passed to the optimizer also improved the predictive accuracy of stiffness, as shown in the final column of the figure. Naturally, including the loss in stiffness in the overall loss function (curves corresponding to  $\mathcal{L}^2$ ) improved the predictive accuracy of the stiffness for both the training and test datasets. Comparing the variants of the loss function, it is evident that including higher-order derivatives of the output function improved the accuracy of the derivative quantities at any given epoch. The substantial improvement in stiffness prediction accuracy is especially beneficial for the downstream finite element algorithm, which would be a typical use case of the ICNN-based model developed here. Consequently, subsequent discussions focus on  $\mathcal{L}^2$  variant only.

**3.2 Numerical Constitutive Model.** At this point, we comment on the accuracy of the trained ICNN for individual components of the desired outputs. We use the normalized MSE, computed as  $\text{NMSE}(y) = \text{MSE}(y)/\text{mean}(y^2)$  as the measure of deviation from the true value. To start, we present the true vs predicted values of the strain energy density function for the test samples in Figure 4. In the figure, the ideal one-to-one match between the true and predicted values is shown using a dotted red line, which has a slope equal to one. The linear regression of the predictions is shown through the solid black line. The computed NMSE for strain energy density is approximately 0.15%, which indicates exceptional predictive accuracy. Similarly, the true vs predicted values for the unique components of the Cauchy stress tensor are shown in Figure 5. The average NMSE for the stress tensor components is 0.815% with a maximum of 1.25% from  $\sigma_{22}$  component.

The mean normalized error increased to 5.4% for the components of the stiffness tensor shown in Figure 6. The maximum deviation was recorded for  $\mathbb{D}_{1312}$  at 23.35%, which is also reflected in the figure as a visible drift of the regression line. The loss of accuracy for stiffness is not necessarily surprising. Two potential reasons are- (i) an amplification of noise due to numerical differentiation techniques used to compute the derivative quantities and (ii) the near-constant gradient of the activation functions at large inputs. The modeling is further complicated by the fact that the underlying data relates to a stochastic fibrous material, which is not guaranteed to have a smooth energy landscape. Despite these challenges, the machine-learned constitutive model is able to faithfully reproduce results on an exemplar Facet Capsular Ligament geometry (Figure 7).

**3.3 Case Study: Uniaxial Tension of FCL.** To demonstrate the efficacy of the ICNN-based model, we present a comparison of results of a boundary value problem with facet capsular ligament geometry (FCL) with the ICNN material model to a full multiscale simulation using MuMFiM. Here we consider “bone” boundary conditions on the left and right surfaces of the facet capsular ligament. That is, the left surface is held encastre and the right surface is fixed in the y and z directions and displaced in the x direction. The meshed geometry and boundary conditions are shown schematically in Figure 7(a).

We consider the result of the same model simulated using MuMFiM as the reference. A more detailed study of this problem is available in [1]. The deformed configurations at approximately 70% global strain obtained from ICNN and MuMFiM based simulations are shown in Figure 7b and 7c, respectively. The color represents the true stress in the elements along the loading di-

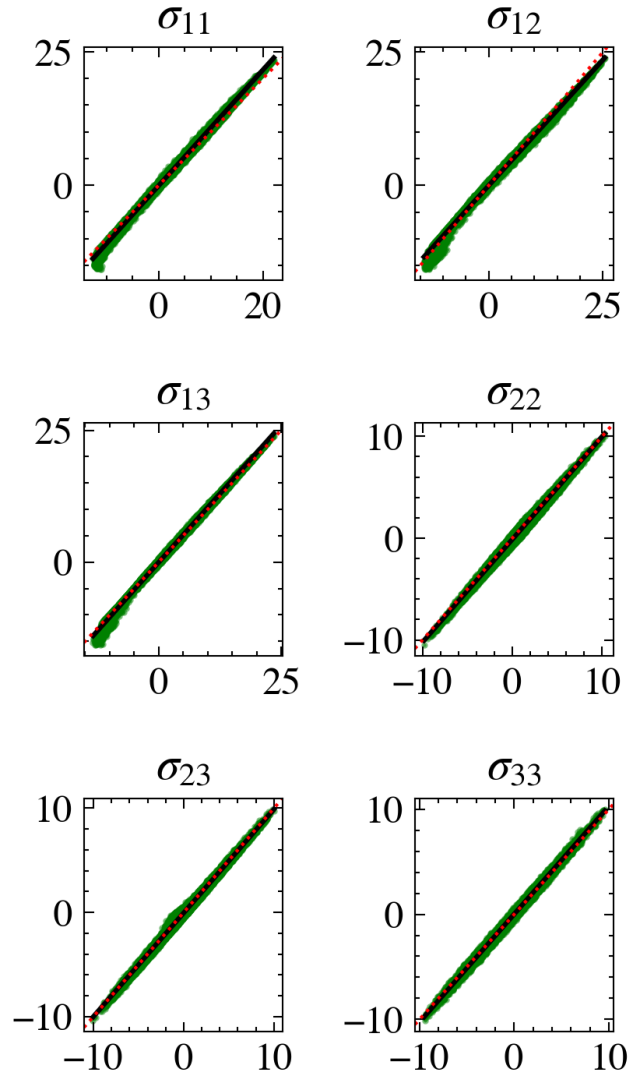


**Fig. 5 True vs predicted values for unique components of Cauchy stress tensor (test set). The component average value of normalized MSE is 0.815%. The result is based on ICNN trained with  $\mathcal{L}^2$  loss function.**

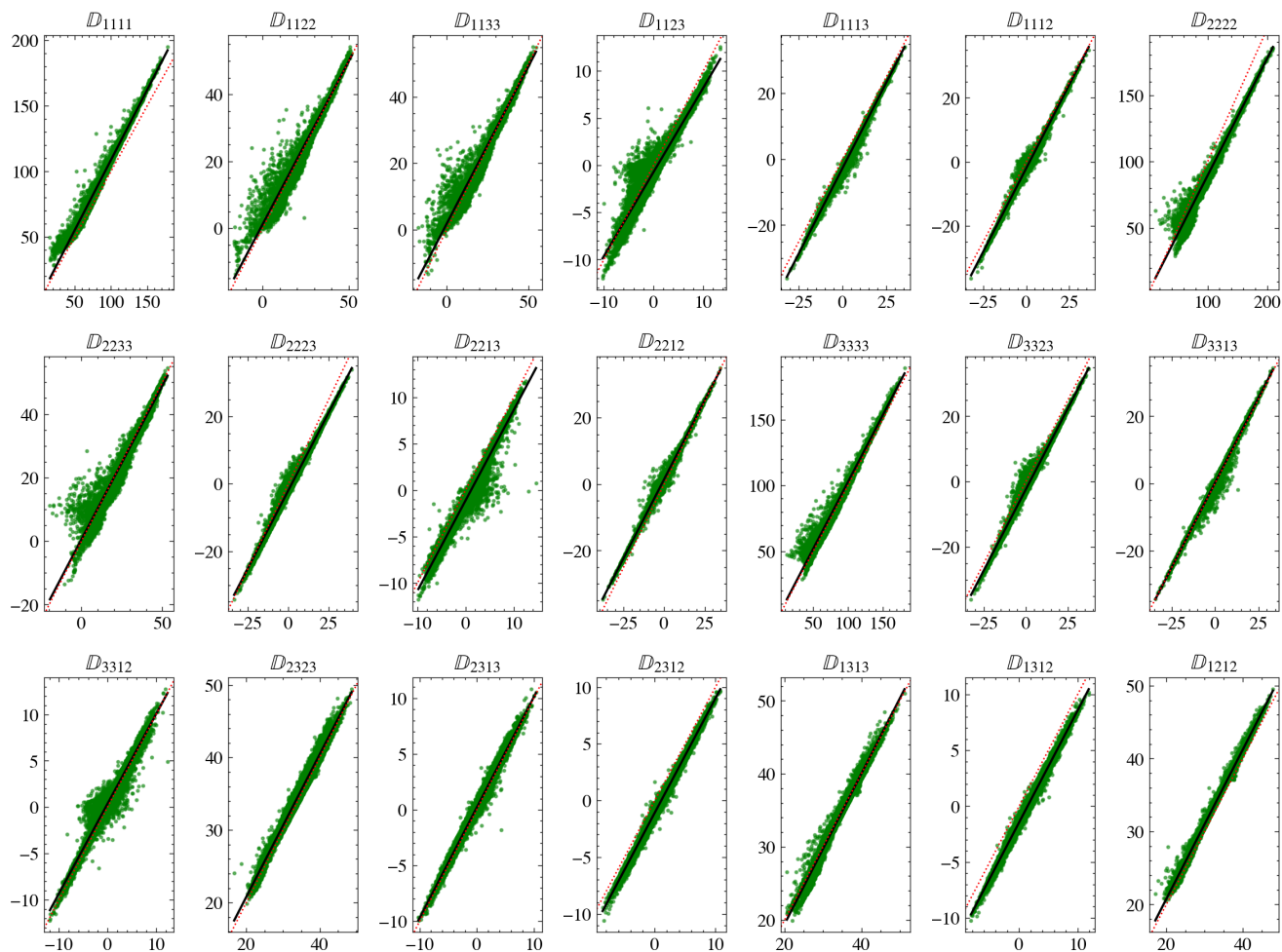


**Fig. 6 True vs predicted values of the unique components of stiffness tensor (test set) based on  $\mathcal{L}^2$  loss function. The average normalized MSE score is 5.4% (maximum: 23%, minimum: 0.03%).**

rection. Visually comparing these results, it is immediately clear that the ICNN-based approach closely replicates the predictions of MuMFiM, including the shear-band-like phenomena appearing due to the geometry of the ligament. We also show the result obtained with a calibrated compressible Neo-Hookean model in 7d. This model predicts a more diffused band with a far smaller maximum stress. Although Neo-Hookean is the simplest material model for hyperelastic behavior, it captures the essence of the difficulties associated with classical continuum models in the context of fibrous network materials. The small parameter space of classical models and strict assumptions regarding the shape of the strain energy density functions fail to capture the complexities arising from the kinematics of the fibers in fibrous materials. A neural network model, such as the one developed here, thus presents a trade-off between explainability and generality.

The stress-strain response of the facet capsular ligament extracted from the MuMFiM and ICNN-based simulation are presented in Figure 8. Both approach predicts exponential stiffening, which is a hallmark behavior of soft biological tissues [21,32,33]. The neo-Hookean model calibrated at the small strain limit is also shown for completeness. The results indicate that the ICNN-based method retains reasonable accuracy up to a very large strain while reducing the computational resource requirement by orders of magnitude- from GPU-accelerated super-computers to consumer-grade laptops. The inset of Figure 8 shows the measured relative error of ICNN-result for stress with respect to MuMFiM. The maximum relative error is in the small-strain regime and upward of 50%. The deviation, however, falls rapidly below 20% at approximately 10% strain. The discrepancy in the small strain regime is related to a similar deviation in the predicted stiffness where the true values are close to zero (Figure 6) and the relative dominance of numerical noise when the true value is small. In fibrous network materials, however, the large strain regime is the principal concern for modeling biological tissues [9]. Given the computational cost for large-scale simulation of fibrous materials and the technical difficulties required to develop efficient algorithms such as those employed in [1], the current model presents an excellent pathway for obtaining approximate results involving the deformation of fibrous materials. Although our work does not obviate the need for large-scale numerical simulations, it does provide a pathway for those in the community to make use of results from those expensive simulations with modest computational resources.

**3.4 Limitations.** The ICNN-based model developed here suffers from several limitations. The major shortcomings are enumerated below.

- (1) *Limited availability of training data:* Our model relies on the higher-order derivatives of the energy function to achieve superior predictive accuracy for quantities such as stiffness tensor components. These datasets are generally not readily available, especially for novel materials. Under these limiting circumstances, we suggest making use of alternative models that rely on available datasets only while being mindful of the loss of accuracy for higher-order quantities.
- (2) *Limited accuracy in stiffness near true zero:* Our model does not enforce  $\mathcal{W} = 0$  for  $\mathbf{F} = \mathbf{I}$  due to the model architecture- specifically, the same constraints that ensure the model convexity. However, the optimizer can adjust the bias in pass-through layers without any constraints to push  $\mathcal{W}$  arbitrarily close to zero. The trained model indeed shows such convergence for strain energy density and stress (Figure 4 and 5) but fails to do so for several components of stiffness tensor. Additionally, the numerical derivatives used to compute the higher-order quantities amplify the noise. We speculate these two factors combined produce this discrepancy.
- (3) *Anticipated loss of accuracy for extreme deformation:* We anticipate the model will gradually lose accuracy beyond the scope of the training dataset. This is particularly important if the problem of interest contains singularities such as sharp

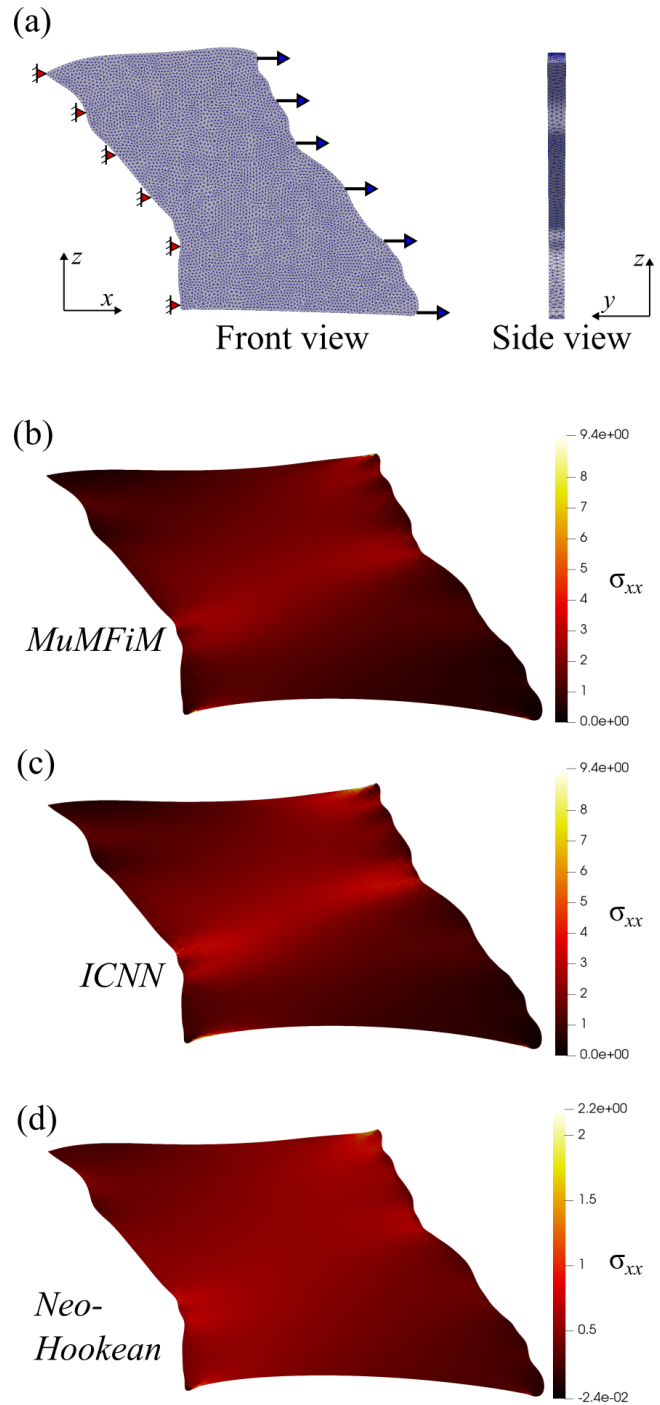


**Fig. 7** (a) Geometry and boundary conditions for numerical simulation of facet capsule ligament (FCL) under uniaxial tension along x-axis. (b) Deformed configuration at 70% strain based on large scale MuMFiM/FE<sup>2</sup> simulation. (c) Deformed configuration at same strain using standard finite element method with trained ICNN ( $\mathcal{L}^2$  variant) as the constitutive descriptor, and (d) with calibrated Neo-Hookean material model. The color indicates the true stress in the elements along the loading direction.

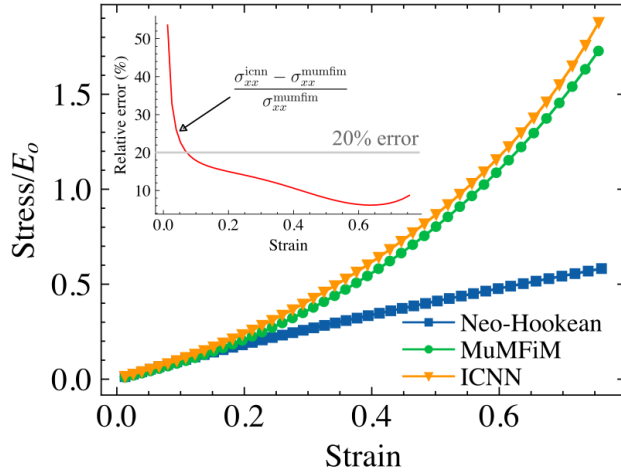


**Fig. 8 True stress as a function of Green-Lagrange strain in the loading direction from on MuMFiM Neo-Hookean, and ICNN-based simulations of FCL under uniaxial tension. The relative error of ICNN-based prediction with respect to MuMFiM is shown as inset.**

cracks. In such use cases, the predictions should be scrutinized carefully, or the model should be re-trained with an extended dataset if necessary.

We hope the published code and dataset will increase interest in this approach and lead to more general models encompassing other material properties, such as fiber pre-alignment and fluctuations.

#### 4 Conclusion

In this paper, we have developed a novel neural network architecture based on an Input Convex Neural Network (ICNN) that is able to accurately predict energies, stresses, and stiffnesses for fibrous materials. This network preserves important constitutive constraints such as polyconvexity and frame indifference through its structure. The strict enforcement of these constraints is critical to obtaining outputs that can be used in well-posed finite element simulations. By construction of higher-order tensor quantities through back-propagation of derivatives, we are additionally able to obtain symmetric stiffness tensors as required by the mathematical description.

We show that constitutive constraints alone are not enough to construct accurate models of stress and stiffness. The incorporation of the Sobolev training protocol, which involves including higher-order derivatives in the loss function, significantly improves the model's prediction accuracy for stress and stiffness. Second, the trained model, when used as a replacement for the microscale segment of the FE2 procedure, provides a quantitatively similar solution to practical problems of interest at a fraction of the computational cost.



## References

- [1] Merson, J. S., Picu, C. R., and Shephard, M. S., 2024, "A New Open-Source Framework for Multiscale Modeling of Fibrous Materials on Heterogeneous Supercomputers," *Engineering with Computers*.
- [2] Mahutga, R. R., Barocas, V. H., and Alford, P. W., 2023, "The Non-Affine Fiber Network Solver: A Multiscale Fiber Network Material Model for Finite-Element Analysis," *Journal of the Mechanical Behavior of Biomedical Materials*, **144**, p. 105967.
- [3] Lai, V. K., Hadi, M. F., Tranquillo, R. T., and Barocas, V. H., 2013, "A Multiscale Approach to Modeling the Passive Mechanical Contribution of Cells in Tissues," *Journal of Biomechanical Engineering*, **135**(7), 071007.
- [4] Holzapfel, G. A., Gasser, T. C., and Ogden, R. W., 2000, "A New Constitutive Framework for Arterial Wall Mechanics and a Comparative Study of Material Models," *Journal of elasticity and the physical science of solids*, **61**(1), pp. 1–48.
- [5] Picu, R. C., Deogekar, S., and Islam, M. R., 2018, "Poisson's Contraction and Fiber Kinematics in Tissue: Insight from Collagen Network Simulations," *Journal of Biomechanical Engineering*, **140**(2), 021002.
- [6] Feyel, F., 1999, "Multiscale FE2 Elastoviscoplastic Analysis of Composite Structures," *Computational Materials Science*, **16**(1), pp. 344–354.
- [7] Merson, J. and Shephard, M. S., 2023, "Using Hierarchical Parallelism to Accelerate the Solution of Many Small Partial Differential Equations," doi: [10.48550/arXiv.2305.07030](https://doi.org/10.48550/arXiv.2305.07030), [2305.07030](https://arxiv.org/abs/2305.07030)
- [8] Merson, J. and Picu, R., 2020, "Size Effects in Random Fiber Networks Controlled by the Use of Generalized Boundary Conditions," *International Journal of Solids and Structures*, **206**, pp. 314–321.
- [9] Picu, C. R., 2022, *Network Materials: Structure and Properties*, 1st ed., Cambridge University Press.
- [10] Hatami-Marbini, H. and Picu, R. C., 2009, "Effect of Fiber Orientation on the Non-Affine Deformation of Random Fiber Networks," *Acta Mechanica*, **205**(1), pp. 77–84.
- [11] Broedersz, C. and MacKintosh, F., 2011, "Molecular Motors Stiffen Non-Affine Semiflexible Polymer Networks," *Soft Matter*, **7**(7), pp. 3186–3191.
- [12] Lake, S. P., Cortes, D. H., Kadlowec, J. A., Soslowky, L. J., and Elliott, D. M., 2012, "Evaluation of Affine Fiber Kinematics in Human Supraspinatus Tendon Using Quantitative Projection Plot Analysis," *Biomechanics and Modeling in Mechanobiology*, **11**(1), pp. 197–205.
- [13] Lee, C.-H., Zhang, W., Liao, J., Carruthers, C. A., Sacks, J. I., and Sacks, M. S., 2015, "On the Presence of Affine Fibril and Fiber Kinematics in the Mitral Valve Anterior Leaflet," *Biophysical Journal*, **108**(8), pp. 2074–2087.
- [14] Thakolkaran, P., Joshi, A., Zheng, Y., Flaschel, M., De Lorenzis, L., and Kumar, S., 2022, "NN-EUCLID: Deep-Learning Hyperelasticity without Stress Data," *Journal of the Mechanics and Physics of Solids*, **169**, p. 105076.
- [15] Sacks, M. S., Motiwale, S., Goodbrake, C., and Zhang, W., "Neural Network Approaches for Soft Biological Tissue and Organ Simulations," *Journal of Biomechanical Engineering*, **144**(121010).
- [16] Kakaletsis, S., Lejeune, E., and Rausch, M. K., "Can Machine Learning Accelerate Soft Material Parameter Identification from Complex Mechanical Test Data?" *Biomechanics and Modeling in Mechanobiology*, **22**(1), pp. 57–70.
- [17] Gupta, A., Bhaduri, A., and Graham-Brady, L., 2023, "Accelerated Multiscale Mechanics Modeling in a Deep Learning Framework," *Mechanics of Materials*, **184**, p. 104709.
- [18] Amos, B., Xu, L., and Kolter, J. Z., 2017, "Input Convex Neural Networks," [1609.07152](https://arxiv.org/abs/1609.07152)
- [19] Glüge, R., 2013, "Generalized Boundary Conditions on Representative Volume Elements and Their Use in Determining the Effective Material Properties," *Computational Materials Science*, **79**, pp. 408–416.
- [20] Kouznetsova, V., Brekelmans, W. A. M., and Baaijens, F. P. T., 2001, "An Approach to Micro-Macro Modeling of Heterogeneous Materials," *Computational Mechanics*, **27**(1), pp. 37–48.
- [21] Parvez, N., Merson, J., and Picu, R. C., 2023, "Stiffening Mechanisms in Stochastic Athermal Fiber Networks," *Physical Review E*, **108**(4), p. 044502.
- [22] Picu, R. and Jin, S., 2023, "Toughness of Network Materials: Structural Parameters Controlling Damage Accumulation," *Journal of the Mechanics and Physics of Solids*, **172**, p. 105176.
- [23] Song, D., Oberai, A. A., and Janmey, P. A., 2022, "Hyperelastic Continuum Models for Isotropic Athermal Fibrous Networks," *Interface Focus*, **12**(6), p. 20220043.
- [24] Tikenogullari, O. Z., Açan, A. K., Kuhl, E., and Dal, H., 2023, "Data-Driven Hyperelasticity, Part II: A Canonical Framework for Anisotropic Soft Biological Tissues," *Journal of the Mechanics and Physics of Solids*, **181**, p. 105453.
- [25] Linden, L., Klein, D. K., Kalina, K. A., Brummund, J., Weeger, O., and Kästner, M., 2023, "Neural Networks Meet Hyperelasticity: A Guide to Enforcing Physics," *Journal of the Mechanics and Physics of Solids*, **179**, p. 105363.
- [26] Tac, V., Sree, V. D., Rausch, M. K., and Tepole, A. B., 2021, "Data-Driven Modeling of the Mechanical Behavior of Anisotropic Soft Biological Tissue," [2107.05388](https://arxiv.org/abs/2107.05388)
- [27] Linka, K. and Kuhl, E., 2023, "A New Family of Constitutive Artificial Neural Networks towards Automated Model Discovery," *Computer Methods in Applied Mechanics and Engineering*, **403**, p. 115731.
- [28] Kingma, D. P. and Ba, J., 2017, "Adam: A Method for Stochastic Optimization," doi: [10.48550/arXiv.1412.6980](https://doi.org/10.48550/arXiv.1412.6980), [1412.6980](https://arxiv.org/abs/1412.6980)
- [29] He, K., Zhang, X., Ren, S., and Sun, J., 2015, "Delving Deep into Rectifiers: Surpassing Human-Level Performance on ImageNet Classification," *Proceedings of the IEEE International Conference on Computer Vision*, pp. 1026–1034.
- [30] Czarnecki, W. M., Osindero, S., Jaderberg, M., Swirszcz, G., and Pascanu, R., "Sobolev Training for Neural Networks,"
- [31] Paszke, A., Gross, S., Massa, F., Lerer, A., Bradbury, J., Chanan, G., Killeen, T., Lin, Z., Gimelshein, N., Antiga, L., Desmaison, A., Kopf, A., Yang, E., DeVito, Z., Raison, M., Tejani, A., Chilamkurthy, S., Steiner, B., Fang, L., Bai, J., and Chintala, S., 2019, "PyTorch: An Imperative Style, High-Performance Deep Learning Library," *Advances in Neural Information Processing Systems*, Vol. 32, Curran Associates, Inc.
- [32] Islam, M. R. and Picu, R. C., 2018, "Effect of Network Architecture on the Mechanical Behavior of Random Fiber Networks," *Journal of Applied Mechanics, Transactions ASME*, **85**(8), pp. 1–8.
- [33] Licup, A. J., Münster, S., Sharma, A., Sheinman, M., Jawerth, L. M., Fabry, B., Weitz, D. A., and MacKintosh, F. C., 2015, "Stress Controls the Mechanics of Collagen Networks," *Proceedings of the National Academy of Sciences of the United States of America*, **112**(31), pp. 9573–9578.

**List of Figures**

1 Schematic of a single Delaunay network (RVE) realization. In the upscaling FEM method, an RVE is solved at every integration point to compute the stress and material stiffness given an increment in macroscale strain. . . . . 2

2 Schematic of input convex neural network. The input vector consists of invariants of the right Cauchy-Green deformation tensor,  $\mathbf{C}$ , and the output is the predicted strain energy density,  $\mathcal{W}$ . The components of true stress,  $\sigma$ , and stiffness tensor,  $\mathbb{D}$ , are computed using automatic differentiation of the trained model. . . . . 3

3 Mean squared error (loss) of ICNN during training. The average errors associated with strain energy density, stress, and stiffness tensors are shown in the first, second, and third column, respectively. The top row shows the loss for the training dataset, and the bottom row represents the corresponding results for the test dataset. The legend  $\mathcal{L}^k := \sum_{i=0}^{i=k} H_i$  indicates the variant of the loss function used to train ICNN, with  $k$  being the highest order of derivative included in the composite loss function. . . . . 4

4 True vs predicted strain energy density for the RVEs (test set) based on ICNN trained with  $\mathcal{L}^2$  loss function. The dashed red line indicates the ideal fit, and the solid black line shows the average trend of the predictions. The value of normalized mean squared error is 0.15% for this dataset. . . . . 4

5 True vs predicted values for unique components of Cauchy stress tensor (test set). The component average value of normalized MSE is 0.815%. The result is based on ICNN trained with  $\mathcal{L}^2$  loss function. . . . . 5

6 True vs predicted values of the unique components of stiffness tensor (test set) based on  $\mathcal{L}^2$  loss function. The average normalized MSE score is 5.4% (maximum: 23%, minimum: 0.03%). . . . . 6

7 (a) Geometry and boundary conditions for numerical simulation of facet capsule ligament (FCL) under uniaxial tension along x-axis. (b) Deformed configuration at 70% strain based on large scale MuMFiM/FE<sup>2</sup> simulation. (c) Deformed configuration at same strain using standard finite element method with trained ICNN ( $\mathcal{L}^2$  variant) as the constitutive descriptor, and (d) with calibrated Neo-Hookean material model. The color indicates the true stress in the elements along the loading direction. . . . . 7

8 True stress as a function of Green-Lagrange strain in the loading direction from on MuMFiM Neo-Hookean, and ICNN-based simulations of FCL under uniaxial tension. The relative error of ICNN-based prediction with respect to MuMFiM is shown as inset. . . . . 8

**List of Tables**